

# Three-Dimensional Quantitative Microwave Imaging of Realistic Numerical Breast Phantoms Using Huber Regularization

Funing Bai<sup>1</sup>, Ann Francois<sup>2</sup>, Jurgen De Zaeytjij<sup>2</sup>, Aleksandra Pižurica<sup>1</sup>

**Abstract**—Breast tumor detection with microwaves is based on the difference in dielectric properties between normal and malignant tissues. The complex permittivity reconstruction of inhomogeneous dielectric biological tissues from microwave scattering is a nonlinear, ill-posed inverse problem. We proposed to use the Huber regularization in our previous work where some preliminary results for piecewise constant objects were shown. In this paper, we employ the Huber function as regularization in the even more challenging 3D piecewise continuous case of a realistic numerical breast phantom. The resulting reconstructions of complex permittivity profiles indicate potential for biomedical imaging.

## I. INTRODUCTION

Recent research [1]–[4] indicates potentials of quantitative microwave imaging (QMWI) to discriminate between tumors and healthy tissue in biomedical imaging. Microwave imaging relies on the capability of microwaves to differentiate among different materials/tissues based on the contrast in their dielectric properties. In biomedical imaging, QMWI quantitatively reconstructs the complex permittivity profile of the biological tissue using microwave scattering measurements. It is well known that the QMWI is a nonlinear and ill-posed inverse problem. Employing appropriate optimization techniques, such as Newton-type methods [5], [6] may address the nonlinearity of the problem. The ill-posedness is treated via regularization, which improves the convergence and stability by reducing the solution space. Different approaches exist for solving this problem. Multiplicative spatial smoothing regularization [5] of the non-linear cost function is applied to a realistic numerical breast phantom in [4]. Multiplicative weighted L2-norm total variation regularization is applied to a human forearm in [7], [8]. The self-regularizing properties of the conjugate gradient least squares (CGLS) algorithm and tissue permittivity bounds are used on realistic numerical breast phantoms in [9].

In this paper, we employ the Huber function as regularization to deal with a challenging case study: 3D reconstructions of the complex permittivity profile from a realistic numerical breast phantom. The Huber function [10]

$$g_{Huber}(\eta) = \begin{cases} \eta^2 & |\eta| \leq \gamma \\ 2\gamma|\eta| - \gamma^2 & \text{else} \end{cases} \quad (1)$$

is quadratic for small  $\eta$  and linear for large values, avoiding in this way over-smoothing at true discontinuities. We

F. Bai and A. Pižurica are with Department of Telecommunications and Information Processing (IPI-TELIN-iMinds), A. Francois and J. De Zaeytjij are with Department of Information Technology (INTEC), Ghent University, Belgium Funing.Bai@telin.ugent.be

proposed to use this function in microwave imaging [11], reconstructing some 3D piecewise constant objects.

Although some initial clinical results of microwave breast imaging have been reported [12], [13], they do not readily lend themselves to rigorous validations of imaging performance. Recent development of realistic MRI-derived numerical phantoms [14], [15] offer more flexibility in capturing the structural complexity of breast tissue than models consisting of arrangements of homogeneous cylindrical or spherical targets. In this paper, we adapt such a realistic breast phantom to a coarser numerical permittivity model which is then illuminated with single frequency microwave fields for data generation. The non-linear least-squares error between these simulated data and the scattered field computed for a current permittivity profile is additively regularized with the Huber function and the resulting cost function is optimized with a Gauss-Newton algorithm with line search.

The results indicate potentials of the proposed Huber regularization in biomedical imaging, and in particular, for applications like breast cancer screening. This paper is organized as follows. Section II introduces the biomedical data and the electromagnetic inverse scattering problem. The proposed method is presented in Section III and breast phantom reconstructions are shown in Section IV.

## II. APPLICATION

### A. Realistic numerical breast phantom

The 3D complex permittivity breast phantom that serves as a testbed in this study is adapted from the UWCEM online Numerical Breast Phantoms Repository [15], which contains a number of anatomically-realistic MRI-derived numerical breast phantoms. As described in [14], these phantoms are obtained from mapping MRIs to a uniform grid of frequency-dependent and tissue-dependent dielectric properties. In this paper, we employ a single-frequency time-harmonic approach (a time dependency  $e^{j\omega t}$ , with  $\omega$  the angular frequency, is assumed), hence the frequency dependency of the complex permittivity is implicit. The (relative) complex permittivity in a point  $\mathbf{r} = (x, y, z)$  then is defined as:

$$\epsilon(\mathbf{r}) = \epsilon'(\mathbf{r}) - j\epsilon''(\mathbf{r}) = \epsilon'(\mathbf{r}, \omega) + \frac{\sigma(\mathbf{r}, \omega)}{j\omega\epsilon_0} \quad (2)$$

where  $\epsilon'$  is the (relative) permittivity and  $\sigma$  the conductivity. In the following, we use permittivity vectors  $\boldsymbol{\epsilon} = \boldsymbol{\epsilon}' - j\boldsymbol{\epsilon}'' = [\epsilon_1, \dots, \epsilon_N]$  on a grid with  $N = N_x \times N_y \times N_z$  cubic cells.

The phantom we selected (Phantom 1, ID:071904, ACR class 1) is a mostly fatty breast phantom with some glandular

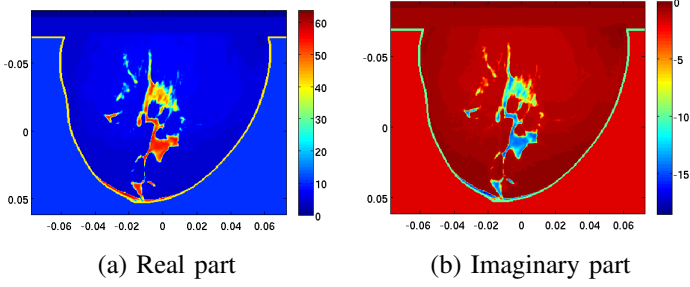


Fig. 1. A view of the permittivity in a slice through the full-resolution MRI-based breast phantom from the online UWCEM repository at 2 GHz.

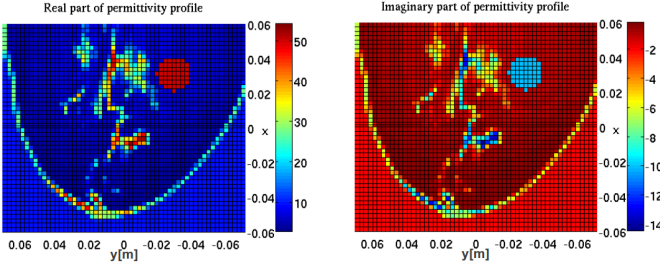


Fig. 2. A view of the permittivity in a slice through the discretized breast phantom for the data generation. The cell size is 2.5 mm, an artificial tumor has been added to the phantom and the muscle layer has been removed.

and fibro-connective inhomogeneities. A slice through this phantom at a frequency of 2 GHz is depicted in Fig. 1. We adapted this high-resolution phantom as follows [4]. As background medium surrounding the breast, we chose a material with permittivity  $10.0 - j2.0$ , which yields a background wavelength  $\lambda_b = 47.2\text{mm}$ . We down sampled the data from a cell-size of 0.5 mm to a cell size of 2.5 mm ( $0.05\lambda_b$ ) by local averaging. An artificial spherical tumor with permittivity  $50.0 - j10.0$  and a radius of 1 cm is inserted manually to position  $(0.03, -0.03, 0)$ , which is rather close to the chest wall. We also removed the muscle layer of the chest wall from the original phantom. This coarser model is depicted in the same slice in Fig. 2 and is used for field data generation in Section IV. The dimensions of this cuboid are  $0.12\text{ m} \times 0.14\text{ m} \times 0.11\text{ m}$  and it contains  $N = 48 \times 56 \times 44 = 118272$  cells.

### B. Electromagnetic inverse scattering problem

A 3D object is illuminated successively with known time-harmonic incident fields from different angles and polarizations and the scattered fields are measured in a number of receiving antennas. Next, a reconstruction algorithm is applied whereby the discretized unknown permittivity profile  $\boldsymbol{\varepsilon} = [\varepsilon_1, \dots, \varepsilon_\nu, \dots, \varepsilon_{N^\varepsilon}]$  is updated iteratively, on a grid with  $N^\varepsilon$  inverse problem cells within a reconstruction domain  $\mathcal{D}$ , by comparing the scattered fields  $\mathbf{e}^{scat}(\boldsymbol{\varepsilon})$  computed in the receiving antenna locations and the measured fields  $\mathbf{e}^{meas}$ . Therefore, the following non-linear cost function is minimized

$$F(\boldsymbol{\varepsilon}) = F^{LS}(\boldsymbol{\varepsilon}) + \mu F^R(\boldsymbol{\varepsilon}) \quad (3)$$

where  $F^{LS}(\boldsymbol{\varepsilon})$  is the least squares data error and  $F^R(\boldsymbol{\varepsilon})$  is a regularization term, with regularization parameter  $\mu \geq 0$ . The least squares data error is

$$F^{LS}(\boldsymbol{\varepsilon}) = \frac{\|\mathbf{e}^{meas} - \mathbf{e}^{scat}(\boldsymbol{\varepsilon})\|^2}{\|\mathbf{e}^{meas}\|^2} \quad (4)$$

where  $\mathbf{e}^{meas}$  and  $\mathbf{e}^{scat}(\boldsymbol{\varepsilon})$  are  $N^d$ -dimensional vectors that contain the field values for all combinations of illuminating and receiving antennas. For the forward problem solution  $\mathbf{e}^{scat}(\boldsymbol{\varepsilon})$  a full-vectorial contrast-source integral equation formulation is adopted and discretized with a Galerkin method of moments on a forward grid ( $N^F$  cells) that is an integer subdivision of the inversion grid ( $N^\varepsilon$  cells); the resulting linear system of equations is solved iteratively with the stabilized bi-conjugate gradient-FFT (BICGSTAB-FFT) method, see [16] for details.

The complex permittivity in iteration  $k$  is updated as  $\boldsymbol{\varepsilon}_{k+1} = \boldsymbol{\varepsilon}_k + \beta_k \Delta \boldsymbol{\varepsilon}_k$ , where  $\beta_k$  is calculated from an approximate line search [17] and  $\Delta \boldsymbol{\varepsilon}_k$  is a Gauss-Newton descent direction obtained from

$$(\mathbf{J}_k^H \mathbf{J}_k + \lambda^2 \boldsymbol{\Sigma}_k^R) \Delta \boldsymbol{\varepsilon}_k = -(\mathbf{J}_k^H [\mathbf{e}^{scat}(\boldsymbol{\varepsilon}_k) - \mathbf{e}^{meas}] + \lambda^2 \boldsymbol{\Omega}_k^{R*}) \quad (5)$$

where  $(\cdot)^H$  stands for Hermitian transpose and  $(\cdot)^*$  denotes the complex conjugate. The trade-off parameter  $\lambda$  is given by  $\lambda^2 = \mu \|\mathbf{e}^{meas}\|^2$  [4]. In the following, the subscript  $k$  is omitted.  $\mathbf{J}$  is the  $N^d \times N^\varepsilon$  Jacobian matrix, which contains the derivatives of the scattered field components with respect to the optimization variables:  $J_{d\nu} = \partial e_d^{scat} / \partial \varepsilon_\nu$ ;  $\boldsymbol{\Omega}_k^{R*}$  is an  $N^\varepsilon$ -dimensional vector that contains the derivatives of the regularizing function and  $\boldsymbol{\Sigma}_k^R$  is a  $N^\varepsilon \times N^\varepsilon$  matrix with second order derivatives. To avoid ill-conditioning of the forward solution, constraints are imposed on the real and imaginary parts of the complex permittivity. These are implemented by a modified, constrained line search [4].

### III. HUBER REGULARIZATION

The regularization term  $F^R(\boldsymbol{\varepsilon})$  in (3) is defined as follows

$$F^R(\boldsymbol{\varepsilon}) = \frac{1}{2} \sum_{\nu} \sum_{\nu' \in N_\nu} g_{Huber}(\varepsilon_\nu - \varepsilon_{\nu'}) \quad (6)$$

where the index  $\nu$  denotes the spatial position  $\nu \equiv (i, j, k)$  and  $N_\nu$  is the neighborhood of  $\nu$ . Let  $\eta$  denote the difference between two neighboring complex permittivities:  $\eta = \varepsilon_\nu - \varepsilon_{\nu'}$ . Considering that  $\eta$  is a complex number, we redefine  $g_{Huber}$  in (6) as

$$g_{Huber}(\eta) = \begin{cases} |\eta|^2 & |\eta| \leq \gamma \\ 2\gamma|\eta| - \gamma^2 & \text{else.} \end{cases} \quad (7)$$

The expressions for the first and second order derivatives of (7), i.e.

$$\boldsymbol{\Omega}^{R*} = \frac{\partial F^R}{\partial \varepsilon_\nu^*} = \sum_{\nu' \in N_\nu} \omega_{\nu'} \quad (8)$$

$$\boldsymbol{\Sigma}_{\nu, \nu'}^R = \frac{\partial^2 F^R}{\partial \varepsilon_\nu \partial \varepsilon_{\nu'}^*} = \sum_{\nu'' \in N_\nu} \sigma_{\nu''} \quad (9)$$

$g_T(\eta)$	$\omega_{\nu'}$	$\varepsilon_\nu - \varepsilon_{\nu'}$	
	$\sigma_{\nu'}$	1	
	$\Sigma_{\nu,\nu'}^R$	-1	
		$ \varepsilon_\nu - \varepsilon_{\nu'}  \leq T_{hr}$	otherwise
$g_H(\eta)$	$\omega_{\nu'}$	$\varepsilon_\nu - \varepsilon_{\nu'}$	$\frac{\gamma(\varepsilon_\nu - \varepsilon_{\nu'})}{ \varepsilon_\nu - \varepsilon_{\nu'} }$
	$\sigma_{\nu'}$	1	$\frac{2 \varepsilon_\nu - \varepsilon_{\nu'} }{\gamma}$
	$\Sigma_{\nu,\nu'}^R$	-1	$-\frac{2 \varepsilon_\nu - \varepsilon_{\nu'} }{\gamma}$

TABLE I

$\omega_{\nu'}$ ,  $\sigma_{\nu'}$  AND  $\Sigma_{\nu,\nu'}^R$ , FOR THE TIKHONOV AND HUBER FUNCTIONS.

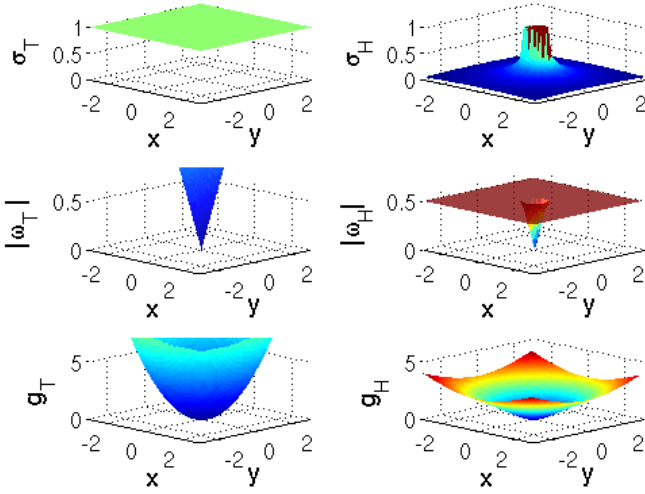


Fig. 3. The qualitative shape of the Huber (right) and Tikhonov (left) functions in the complex domain.

for the diagonal elements and

$$\Sigma_{\nu,\nu'}^R = \frac{\partial^2 F^R}{\partial \varepsilon_{\nu'} \partial \varepsilon_\nu^*} \quad (10)$$

for the non-diagonal elements of  $\Sigma^R$  (which are zero except if  $\nu' \in N_\nu$ ), were derived in [11] and are summarized in TABLE I. The table also shows the expressions for Tikhonov regularization,  $g_T(\eta) = |\eta|^2$ , which is employed as a benchmark in Section IV, using 3 nearest neighbors for  $N_\nu$  and replacing  $g_H$  with  $g_T$  in (6) (i.e. L2 norm total variation) within the Multiplicative Smoothing (MS) regularization technique [5]. Note that with MS, the cost function is given by  $F = F^{LS} (1 + \mu F^R)$ . Fig. 3 illustrates the Huber function  $g_H(\eta)$  and the Tikhonov function  $g_T(\eta)$  in the complex domain ( $\eta = \alpha + j\beta$ ), together with the corresponding magnitude  $|\omega(\eta)|$  and  $\sigma(\eta)$  functions. Note that  $|\omega|$ , which is an indication of the smoothing strength, increases monotonically with  $|\eta|$  in the whole domain of  $|\omega_T|$ , whereas  $|\omega_H|$  only does so in the smoothing interval  $|\eta| < \gamma$  and remains a constant, allowing limited (bounded) smoothing, outside this interval. The interaction  $\sigma$ , which determines the interaction between neighboring pixels also

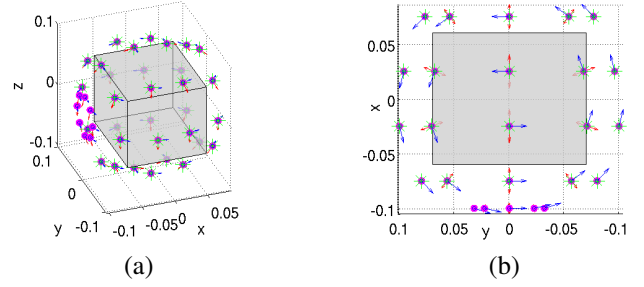


Fig. 4. Antenna positions (dots) on a hemi-ellipsoidal-like surface. The arrows in two orthogonal directions indicate transmitting dipoles. The cuboid in the center indicates the reconstruction domain  $\mathcal{D}$ . (a) xyz view; (b) xy view.

behaves differently for the two regularizations:  $\sigma_H$  is smaller for large  $|\eta|$  and approaches 0 as  $|\eta|$  goes to  $\infty$ , while  $\sigma_T$  holds the same interaction power in the whole domain. This way, the Huber function preserves edges and reduces the effect of outliers. A pseudo-code of the reconstruction algorithm is given in [11].

#### IV. RESULTS AND DISCUSSION

In this section we show reconstructions of the numerical breast phantom using Huber regularization and compare with reconstructions obtained with Tikhonov regularization employed in a multiplicative way (MS) [4].

Synthetic scattered field data are computed at 2 GHz with the forward solver [16] for the numerical phantom of Fig. 2. Since a breast is attached to a body, hence it is not a free-standing object, the antennas cannot be located all around it, as with the spherical configurations in [11]. We choose a configuration as in Fig. 4, where antennas are positioned on 5 circles on an hemi-ellipsoidal-like surface around the front side of a gray cuboid. The cuboid contains the breast phantom with the chest wall in the  $yz$ -plane at  $x = 0.06$  m. The 5 circles, which are centered on the  $x$ -axis and parallel to the  $yz$ -plane, each contain 8 equally spaced antenna positions with in each position 2 dipoles with polarizations in two orthogonal directions tangential to the spheroid. This yields a total of 80 dipoles, which is only half of the number used in [4], hence requiring less computational effort. All 80 dipoles are used to sample the field, but only 64 of them (indicated with the larger green dots) are used to illuminate the phantom. This yields a total of  $N^D = 5120$  complex field values. A SNR of 30 dB additive Gaussian noise is applied.

The reconstruction domain  $\mathcal{D}$  (gray cuboid) in the inverse solver is discretized in  $N^\varepsilon = 24 \times 28 \times 22$  cubic cells with size 5 mm, yielding a total of 14784 complex permittivity unknowns. This means that the problem is heavily under-determined. To test the abilities of the method, we perform a complete blind reconstruction, i.e. we do *not* use *a-priori* knowledge of the breast contour, which is sometimes suggested in the literature. Hence, the initial estimate is just the uniform background medium with permittivity  $10 - j2$ . To keep the forward problems well-conditioned (which are

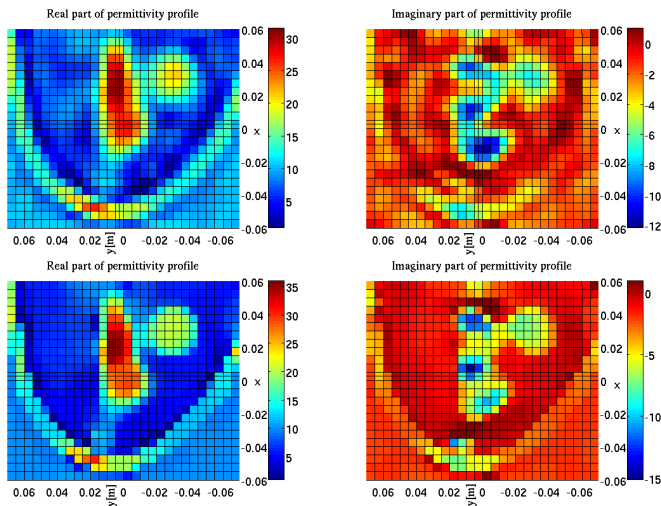


Fig. 5. Breast phantom reconstruction showing the real parts (left) and imaginary parts (right) of the complex permittivity profile. Top: MS reconstruction; Bottom: Huber regularization.

solved on the grid with cell size 2.5mm), the constraints on the permittivity are  $1.0 < Re(\epsilon) < 55.0$  and  $-50.0 < Im(\epsilon) < 1.0$ . The tolerance for the BICGSTAB iterative routine is set to  $10^{-3}$ . We optimized the regularization parameter  $\mu$  and the parameter  $\gamma$  of the Huber function experimentally for satisfactory edges. We obtained the same optimal value ( $\mu \approx 10^{-6}$ ) for different targets and antenna configurations. For continuous profiles (like in biomedical applications) a smaller value for  $\gamma$  than with piecewise constant objects should be used:  $\gamma = 10^{-2}$ . The regularization parameter for MS is set to  $\mu = 10^{-4}$  [4]. For the neighborhood  $N_\nu$  with  $g_H$  in (6), we used 26 nearest neighbors in 3D as a compromise between reconstruction quality and complexity. All computations were performed on a six-core Intel i7 980x processor (3.33GHz) with 24GByte memory.

Fig. 5 shows the real and imaginary parts in one slice through the reconstructed complex permittivity profile for Huber (bottom) and Tikhonov [4] (top). The shape of the breast and the locations and dimensions of the healthy heterogeneities and of the tumor are well reconstructed in all images. The real parts are rather similar, although the MS image shows a more smoothed tumor: for both regularization methods the permittivity of the tumor (and of the other tissues) is too low compared to the reference in Fig. 2. There are more differences between both methods in the imaginary parts: the breast contour and the tumor appear clearer with Huber but the inner glandular tissue heterogeneities are more distinguished with MS. The reconstructions were stopped after 13 iterations and took less than 1 hour.

## V. CONCLUSIONS

In this paper, we applied the Huber regularization to biomedical data for quantitative microwave imaging. The method is able to reconstruct the spatial complex permittivity distribution in biological objects from blind reconstruction at one single frequency, thereby overcoming difficulties with

the dispersive nature of body tissues. Numerical results indicate the potentials of the method for breast tumor detection even though a thorough analysis for this challenging problem still needs to be done.

## ACKNOWLEDGMENT

The authors wish to thank Yanlu Li from the Photonics Research group at Ghent University for discussing data transformation from UWCEM. This work was supported by the Fund for Scientific Research Flanders (F.W.O.-Vlaanderen).

## REFERENCES

- [1] D. Winters, J. Shea, P. Kosmas, B. Van Veen, and S. Hagness, "Three-dimensional microwave breast imaging: Dispersive dielectric properties estimation using patient-specific basis functions," *IEEE Trans. Med. Imaging*, vol. 28, no. 7, pp. 969–981, July 2009.
- [2] T. Henriksson, N. Joachimowicz, C. Conessa, and J.-C. Bolomey, "Quantitative microwave imaging for breast cancer detection using a planar 2.45 GHz system," *IEEE Trans. Instrum. Meas.*, vol. 59, no. 10, pp. 2691–2699, Oct. 2010.
- [3] A. Fhager, M. Gustafsson, and S. Nordebo, "Image reconstruction in microwave tomography using a dielectric Debye model," *IEEE Trans. Biomed. Eng.*, vol. 59, no. 1, pp. 156–166, Jan 2012.
- [4] J. De Zaeytjij, "On the 3D electromagnetic quantitative inverse scattering problem: algorithms and regularization," Ph.D. dissertation, Ghent University, 2009.
- [5] J. De Zaeytjij, A. Franchois, C. Eyraud, and J.-M. Geffrin, "Full-wave three-dimensional microwave imaging with a regularized Gauss-Newton method - theory and experiment," *IEEE Trans. Antennas Propag.*, vol. 55, no. 11, pp. 3279–3292, Nov. 2007.
- [6] T. Rubk, P. Meaney, P. Meincke, and K. Paulsen, "Nonlinear microwave imaging for breast-cancer screening using Gauss-Newton's method and the CGLS inversion algorithm," *IEEE Trans. Antennas Propag.*, no. 8, pp. 2320–2331, Aug. 2007.
- [7] A. Abubakar, P. van den Berg, and J. Mallorqui, "Imaging of biomedical data using a multiplicative regularized contrast source inversion method," *IEEE Trans. Microw. Theory and Tech.*, vol. 50, no. 7, pp. 1761–1771, Jul 2002.
- [8] P. Mojabani and J. LoVetri, "Enhancement of the Krylov subspace regularization for microwave biomedical imaging," *IEEE Trans. Med. Imaging*, vol. 28, no. 12, pp. 2015–2019, 2009.
- [9] J. D. Shea, P. Kosmas, S. C. Hagness, and B. D. Van Veen, "Three-dimensional microwave imaging of realistic numerical breast phantoms via a multiple-frequency inverse scattering technique," *Med. Phys.*, vol. 37, no. 8, pp. 4210–4226, 2010.
- [10] P. J. Huber, "Robust regression: Asymptotics, conjectures and Monte Carlo," *The Annals of Statistics*, vol. 1, no. 5, pp. 799–821, 1973.
- [11] F. Bai, A. Pižurica, S. Van Loocke, A. Franchois, D. De Zutter, and W. Philips, "Quantitative microwave tomography from sparse measurements using a robust Huber regularizer," in *In IEEE Int. Conf. Image Processing (ICIP)*, October 2012, pp. 2073–2076.
- [12] M. Klemm, I. Craddock, J. Leendertz, A. Preece, and R. Benjamin, "Experimental and clinical results of breast cancer detection using UWB microwave radar," in *Antennas and Propagation Society International Symposium, 2008. AP-S 2008. IEEE*, July 2008, pp. 1–4.
- [13] P. M. Meaney, M. W. Fanning, T. Reynolds, C. J. Fox, Q. Fang, C. A. Kogel, S. P. Poplack, and K. D. Paulsen, "Initial clinical experience with microwave breast imaging in women with normal mammography," *Acad. Radiol.*, vol. 14, no. 2, pp. 207–218, 2007.
- [14] E. Zastrow, S. Davis, M. Lazebnik, F. Kelcz, B. Van Veen, and S. Hagness, "Development of anatomically realistic numerical breast phantoms with accurate dielectric properties for modeling microwave interactions with the human breast," *IEEE Trans. Biomed. Eng.*, vol. 55, no. 12, pp. 2792–2800, Dec. 2008.
- [15] UWCEM. numerical breast phantom repository. [Online]. Available: <http://uwcem.ece.wisc.edu>
- [16] J. De Zaeytjij, I. Bogaert, and A. Franchois, "An efficient hybrid MLFMA-FFT solver for the volume integral equation in case of sparse 3D inhomogeneous dielectric scatterers," *J. Comput. Phys.*, vol. 227, pp. 7052–7068, July 2008.
- [17] R. Fletcher, *Practical methods of optimization; (2nd ed.)*. New York, NY, USA: Wiley-Interscience, 1987.